

Extending Daytime Adaptive Optics to Faint Objects

Michael Hart

HartSCI LLC, 2555 N. Coyote Dr. #114, Tucson, AZ 85745, USA

Abstract

Custody and characterization of satellites during the day is enormously challenged by the photon noise introduced by the bright daytime sky. In particular, daytime use of adaptive optics (AO) at large telescopes is generally infeasible because of noise or saturation of the wavefront sensor. That problem may be overcome through use of a sodium laser guide star observed through a magneto-optical filter to suppress the background, but the laser beacon is not sensitive to overall image motion. To estimate wavefront tilt, laser-guided AO systems generally rely on light from the object itself, collected through the full aperture of the telescope. Daylight sets a lower limit to the brightness of an object that may be tracked at rates sufficient to overcome the image jitter. Below that limit wavefront correction on the basis of the laser alone will yield an image that is approximately diffraction limited, but that moves randomly. I describe a new registration algorithm that recovers high-resolution long exposure images in this regime from a rapid series of short exposures with very low signal-to-noise ratio. The technique takes advantage of the fact that in the photon noise limit there is negligible penalty in taking short exposures, and that both past and future history are available to the registration algorithm. The algorithm is likely to find application in space situational awareness, where it is expected to enable access at high resolution to objects as faint as magnitude 12.

Keywords: adaptive optics, atmospheric turbulence, wavefront sensing, daylight imaging.

1 Introduction

AO systems on large telescopes used for space situational awareness (SSA) are presently challenged during daylight operation. The seeing is typically worse than at night because of thermal plumes arising from solar heating of the ground. The wavefront sensor (WFS) suffers from shot noise in the bright sky background, and may also simply saturate, preventing it from providing any useful information.

Beckers and Cacciani¹ suggested in 2001 that the value of extremely large astronomical telescopes of 25 m and bigger could be extended by using them with laser-guided AO at thermal infrared wavelengths during the day since the limitation imposed by the sky background in these bands is no worse than at night. They described a practical daytime AO system that could be implemented with a sodium laser guide star (LGS) when the WFS employs a magneto-optical filter (MOF).²⁻⁴ A MOF offers a transmission profile of typically just 10 pm width⁵ which passes the LGS light with high efficiency but blocks light at all other wavelengths, very effectively reducing the sky background. We have recently shown experimentally that the combination of a sodium LGS and MOF is viable for daytime AO wavefront sensing.⁶

The same method may be used to support high-resolution daytime imaging of artificial satellites.⁷ Observations of low-Earth orbit satellites now are largely restricted to so-called terminator mode around dawn and dusk when the satellite is sunlit but the sky is still dark. It is presently also very challenging to observe an important class of objects in sun-synchronous orbits which always appear over a given site at the same time of day.

It is well known that global wavefront tilt cannot be estimated from LGS signals because of the unknown beam wander on the upward path. Generally an independent tracking camera is used, looking at light from the object of interest itself or in astronomical usage a nearby reference star. But what if no suitable object is available? High-order wavefront corrections applied by reference to the LGS with no tip-tilt correction will result in an image that is instantaneously close to diffraction limited, but that moves around in the focal plane on the scale of the atmospheric coherence time τ_0 .⁸ At very large telescopes the effect of a finite outer scale of turbulence may admit modest correction even without a tip-tilt star.⁹ But on telescopes of a few meters' diameter or less a single exposure substantially longer than τ_0 will be blurred almost as badly as if no AO correction had been applied at all. Yet, as the object becomes fainter, the only way to maintain a given signal-to-noise ratio (SNR) in the presence of high background illumination is to accumulate signal over longer periods. This is a fundamental physical limitation.

Imaging at visible wavelengths during the day is an extreme background-limited case where many objects of interest will be too faint to be tracked with sufficient speed and accuracy to correct image motion in real time. On the other hand, in this regime even short exposures that freeze the motion will be dominated by background shot noise rather than read noise from the detector. With negligible noise penalty, then, one can consider a scheme whereby a long exposure image is synthesized from a sequence of short exposures with the motion of the object computed by an image registration algorithm and applied as image shifts in the computer. This is already a well-known paradigm in the AO community. Robo-AO is an example of a laser-guided AO system that successfully exploits it, using a standard cross-correlation between each frame and a theoretical point-spread function.¹⁰ Many other algorithms have been developed for image registration, based for example on maximum likelihood estimation^{11,12} under the assumption of various noise models.

In a previous paper I proposed a new algorithm that demonstrates robustness under conditions of very low SNR and that makes no assumptions about the noise model.¹³ Here I describe an improved version that more rigorously delivers an optimal solution. The algorithm relies on a key difference between real-time motion correction and numerical image registration that allows the latter to succeed where the former may fail: both past and future history are available to the registration algorithm. The method described here exploits that fact under the assumption that the object appears the same in all frames.

2 Algorithm Development

The distinguishing characteristic of a good coadded image stack, where the image shifts are well estimated, compared to a bad one is the power in angular frequencies between the seeing limit $f_{SL} = r_0/\lambda$ and the diffraction limit $f_{DL} = D/\lambda$, where r_0 is the atmospheric coherence length, D

is the telescope diameter, and λ is the mean wavelength of observation. Outside this range, angular frequencies are not diagnostic of the image shifts. The uncorrected image motion does not degrade frequencies below f_{SL} , and those higher than f_{DL} are attributable solely to noise. The algorithm finds image shifts that maximize the power spectrum of the coadded image within this range.

A metric ε is defined as the sum of the power spectrum of the coadded image stack over an annulus between f_{SL} and f_{DL} . Image shifts ξ_k, v_k are sought to maximize ε according to

$$\arg \max_{\xi_k, v_k} \varepsilon = \sum_{\substack{u^2+v^2 < f_{DL}^2 \\ u^2+v^2 > f_{SL}^2}} \left\| \mathcal{F} \left(\sum_k I_k(x + \xi_k, y + v_k) \right)_{u,v} \right\|^2. \quad (1)$$

In Eq. 1, $|\cdot|$ represents the modulus, $\mathcal{F}()$ is the Fourier transform, I_k is the k th image in the sequence, and (u, v) and (x, y) are coordinates in the Fourier plane and image plane respectively.

Finding the solution to Eq. 1 in a space of high dimensionality is challenging. The results presented in Section 4 relied on a gradient descent algorithm based on the `firpmn` method¹⁴ which requires the derivatives of the metric with respect to the optimization variables. If the complex-valued Fourier transform of image I_k is $a_k(u, v)e^{i\phi_k(u,v)}$ then

$$\varepsilon = \sum_{u,v} W(u, v) \left\| \sum_k a_k(u, v) e^{i(\phi_k(u,v) + u\Xi_k + v\Upsilon_k)} \right\|^2$$

Here, Ξ_k and Υ_k are the tilt angles applied to the phases of the transform of image I_k , according to the Fourier shift theorem, to move the image in real space. That is, $\Xi_k = 2\pi\xi_k/D$, $\Upsilon_k = 2\pi v_k/D$ when the image plane coordinates (x, y) are expressed in angular units of the diffraction limit λ/D . W is a window function specifying the range of spatial frequencies of interest, defined as

$$W(u, v) = \begin{cases} 1 & f_{SL}^2 < u^2 + v^2 < f_{DL}^2, \\ 0 & \text{otherwise.} \end{cases} \quad (2)$$

Now, to maximize ε , we seek Ξ_k and Υ_k such that

$$\left. \frac{\partial \varepsilon}{\partial \Xi} \right|_{\Xi_k, \Upsilon_k} = \left. \frac{\partial \varepsilon}{\partial \Upsilon} \right|_{\Xi_k, \Upsilon_k} = 0. \quad (3)$$

Computing the derivatives with respect to a particular image shift:

$$\begin{aligned} \frac{\partial \varepsilon}{\partial \Xi_k} &= -2 \sum_{u,v} W \sum_{l \neq k} u a_k a_l \sin[\phi_k - \phi_l + u(\Xi_k - \Xi_l) + v(\Upsilon_k - \Upsilon_l)] \\ \frac{\partial \varepsilon}{\partial \Upsilon_k} &= -2 \sum_{u,v} W \sum_{l \neq k} v a_k a_l \sin[\phi_k - \phi_l + u(\Xi_k - \Xi_l) + v(\Upsilon_k - \Upsilon_l)]. \end{aligned}$$

Here and henceforward the explicit (u, v) indexing of the amplitude and phase variables is omitted for clarity. These equations are conveniently written in terms of the cross-correlation between images I_k and I_l .

$$\begin{aligned}
\frac{\partial \varepsilon}{\partial \Xi_k} &= -2 \sum_{l \neq k} \text{Im} \left\{ \mathcal{F}^{-1}(Wu \mathcal{F}(I_k \star I_l)) \right\} \\
&= -2 \sum_{l \neq k} \text{Im} \left\{ \mathcal{F}^{-1}(Wu) \right\} \odot (I_k \star I_l) \Big|_{\Delta \Xi_{kl}, \Delta \Upsilon_{kl}} \\
\frac{\partial \varepsilon}{\partial \Upsilon_k} &= -2 \sum_{l \neq k} \text{Im} \left\{ \mathcal{F}^{-1}(Wv \mathcal{F}(I_k \star I_l)) \right\} \\
&= -2 \sum_{l \neq k} \text{Im} \left\{ \mathcal{F}^{-1}(Wv) \right\} \odot (I_k \star I_l) \Big|_{\Delta \Xi_{kl}, \Delta \Upsilon_{kl}}
\end{aligned} \tag{4}$$

where \odot represents convolution. The variables of the inverse Fourier transforms are $\Delta \Xi_{kl} = \Xi_k - \Xi_l$ and $\Delta \Upsilon_{kl} = \Upsilon_k - \Upsilon_l$; the derivatives of the metric with respect to each shift variable depend on all of them.

One observes that Eq. 4 applies a filter function to the pair-wise cross-correlations of the images. Since W is an annulus, the filter looks something like the Airy pattern of a conventional telescope's point-spread function. Examples calculated for a specific geometry are shown in Fig. 1. It is apparent that the derivative is essentially computed from local centroids within the cross-correlated images; regions of maximal (and minimal) correlation will show zero centroid values.

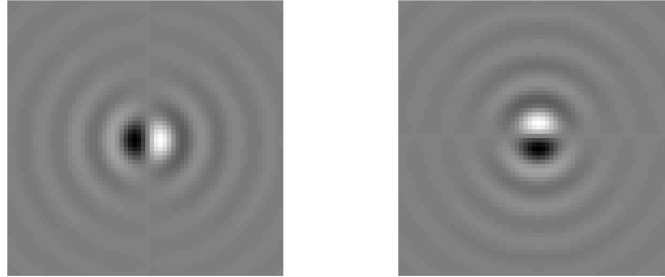


Fig 1 Filter functions applied to the pair-wise cross-correlations of the images.

The surface defined by the metric in Eq. 1 will in general have many local maxima and the gradient descent algorithm will tend to get stuck on one of them rather than finding the desired global maximum. To guard against this, an additional term is included in the cost function that penalizes large differences between adjacent shift values, $\langle |\Xi_k - \Xi_{k+1}|^2 + |\Upsilon_k - \Upsilon_{k+1}|^2 \rangle$.

3 Data

The method has been tested with simulated data constructed from a real sequence of observations of the Hubble Space Telescope (HST) made with the AO system at the 3.6 m Advanced Electro-Optical System (AEOS) telescope on Mt. Haleakala, Hawaii.¹⁵ The sequence comprised 250

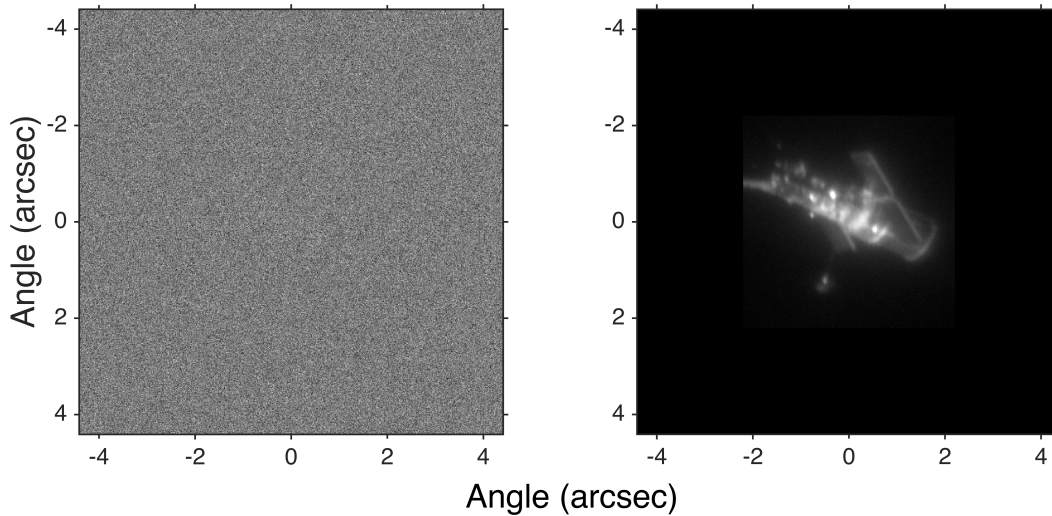


Fig 2 One of the AO-corrected images from the sequence collected at the AEOS telescope and used in this study. (Left) with simulated added noise; (right) the original image shown on a square-root scale.

contiguous 512×512 frames with 2 ms exposure recorded through an optical filter centered at approximately 800 nm. The images are close to diffraction limited; an example is shown on the right of Fig. 2.

To make the simulated data, the recorded sequence was replicated ten times to form a sequence 2,500 frames long. Image motion was modeled by shifting each frame, using the Fourier shift theorem, according to two sequences of pseudo-random values obeying Kolmogorov statistics for wavefront tilt. The values, plotted in Fig. 3, were scaled to a standard deviation of 0.25 arcsec, the expected value for $r_0 = 10$ cm at 500 nm.¹⁶ Each frame was then convolved with a line representing the motion vector between itself and the next frame in the sequence. This procedure crudely models the residual motion blur to be expected when the object is not actively tracked by an AO system. The mean images, averaged over the full sequence, with and without the artificial image shifts are shown in Fig. 4. Fig. 5 illustrates the difference in spatial frequency content in the two coadded images, quantified in Eq. 1. Finally, photon noise was added assuming an integrated I-band object brightness of $m_{obj} = 9$ and sky background surface brightness of $m_{sky} = 4$ arcsec⁻².^{17,18} For completeness, gaussian detector read noise of 3 electrons rms was also added, although the contribution is negligible in comparison to the shot noise: the mean sky background per pixel was 304 photons. The model parameters are summarized in Table 1.

The left panel of Fig. 2 shows one of the modeled data frames: the object has all but disappeared. The mean object flux per frame is 10,300 photons, leading to a SNR per illuminated pixel of less than 0.03. For the entire object, the SNR is about 4.

4 Results

The results of applying the image motion correction algorithm to the HST data are shown in Fig. 6. The result is encouraging: compared to the true positions in Fig. 3 the residual is 0.032 arcsec

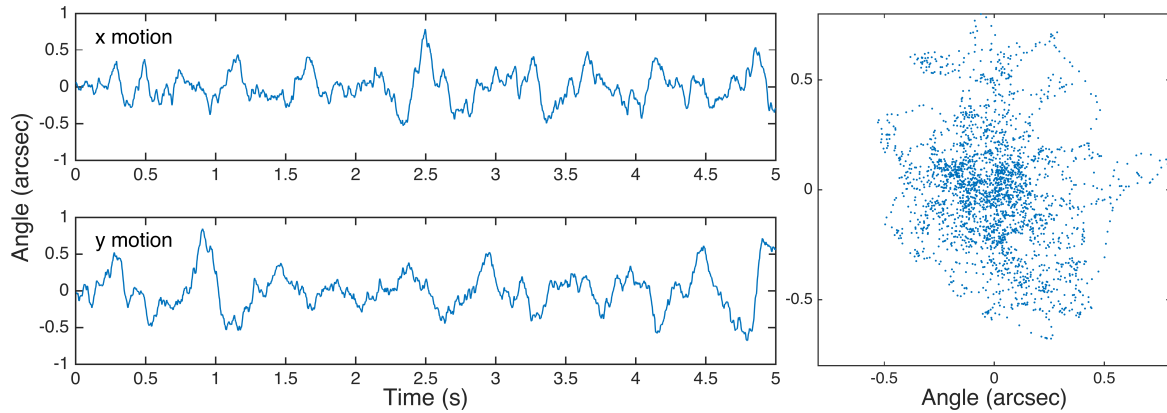


Fig 3 The random motion assigned to the 2,500 data frames, modeling 5 s of elapsed time at 2 ms per frame, shown as linear plots (left) and a scatter plot (right).

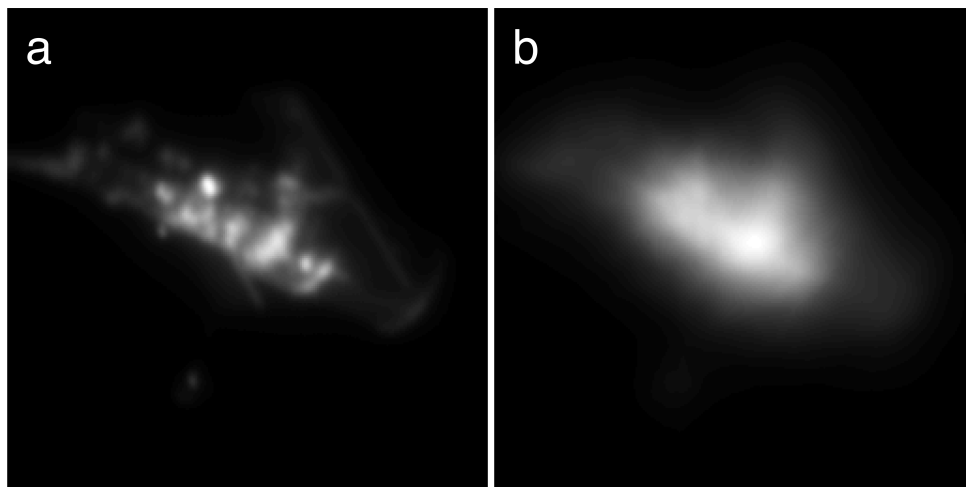


Fig 4 Averages of the 2,500 frame sequences before the addition of noise. (a) Unshifted frames. (b) Shifted frames. Both images on linear gray scale.

Table 1 Parameters of the simulated data

| Parameter | Value |
|-------------------------------------|--|
| Telescope diameter | 3.6 m |
| Overall optical efficiency | 25% |
| Center wavelength | 800 nm |
| Optical bandwidth | 22% |
| Atmospheric coherence length r_0 | 10 cm at 500 nm |
| Atmospheric coherence time τ_0 | 1 ms at 500 nm |
| Filter magnitude zero point | 8.0×10^9 photon $\text{m}^{-2} \text{s}^{-1}$ |
| Object brightness | $m_{obj} = 9$ |
| Sky brightness | $m_{sky} = 4$ arcsec $^{-2}$ |
| Detector read noise | $3e^-$ rms |
| Integration time | 2 ms |
| Pixel scale | 0.0172 arcsec |

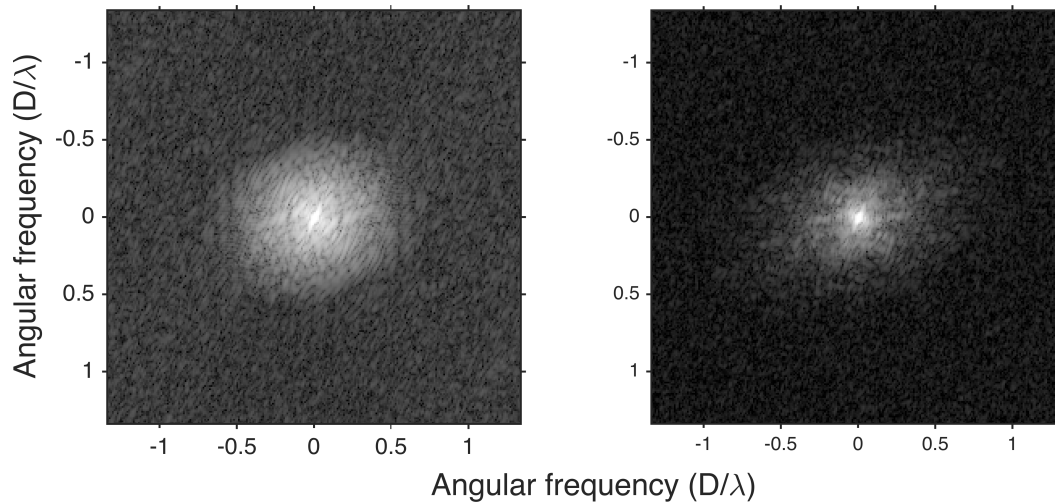


Fig 5 Square root of the power spectrum of the noise-free HST images. (Left) Original AO corrected frames. (Right) With artificial shifts. Both images on same logarithmic scale.

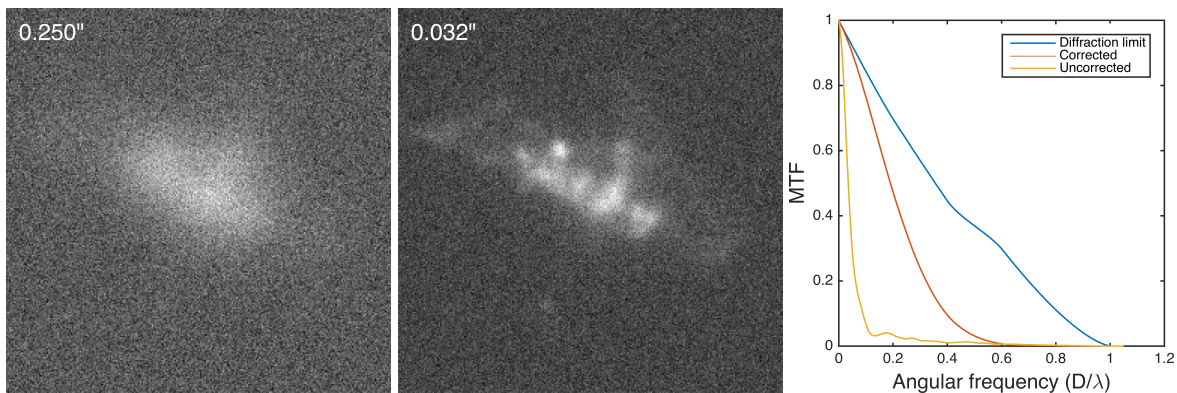


Fig 6 Results of the image shift computation. (Left) Mean image before any correction. (Center) Result after image motion compensation. The number at top of each frame quantifies the rms residual single-axis position error. (Right) Plots of the rotationally-averaged MTF for the corrected and uncorrected cases compared to the diffraction limit.

or $0.70 \lambda/D$. The final image has a resolution close to the diffraction limit. This is quantified by the plots in Fig. 6 which show the modulation transfer function (MTF), averaged azimuthally, for the corrected and uncorrected cases as well as for the diffraction limit. The MTFs were calculated from simulated noise-free point source images subjected to the same shifts as the HST data frames.

In the case simulated here the object is too faint for effective real-time tip-tilt correction. Given the SNR for detection, we should expect that the accuracy of tip-tilt estimation from a single frame would be $1/4$ the object's extent, or about 1.0×0.4 arcsec along and across the body of the HST. That is already coarser than the entire atmospheric tilt error of 0.25 arcsec rms. Attempting to integrate past data would not help: to achieve the SNR needed to match the residual tilt error of 0.032 arcsec found by post-processing would require a look-back of over 500 frames, or more than 1 second. That is long enough that the atmospheric tilt will explore its full range, preventing any precise measurement.

5 Conclusions

The algorithm is not real time. On a 2016 MacBook Pro, it takes about 20 minutes to find the optimal shifts for the 2,500 frame HST simulation, with most of that time spent finding the shifts and about 3 minutes actually recentering the images. It is likely that a significant speed increase could be realized by approaching the problem hierarchically. The problem may be divided into smaller subsets where the range of motion will be constrained, since the atmospheric image motion approximately follows a power law. Images within each subset could be shifted, binned, and then treated as the input frames to a next stage of computation. The goal at each stage is to give the gradient descent algorithm a starting point that is as close as possible to the solution.

A thorough analysis of the performance of the algorithm would account for the spectrum of the object since that has a direct effect on the sensitivity of ε to changes in the image shifts. It is unlikely that the object spectrum will be known in advance but one may still estimate from general considerations the minimum surface brightness where the method will have some value.

For significant improvement, we should expect to require that the object be detectable within each frame at $\text{SNR} > 1$. Insisting that the total object signal per frame exceed the sky noise from the same solid angle Ω leads to the requirement

$$F_{obj} \gtrsim (F_{sky}/\tau_0)^{1/2} D^{-1} \Omega^{-1/2} \quad (5)$$

where F_{obj} and F_{sky} are respectively the object and sky fluxes in $\text{photon s}^{-1} \text{ m}^{-2} \text{ rad}^{-2}$ received at the detector, and the frame integration time is assumed to be τ_0 . In the spirit of the approximation I neglect factors of order unity, and the terms highlight respectively the temporal, spatial, and angular dependencies. As one would expect, larger diameter telescopes have a clear advantage.

The HST simulation modeled a source of solid angle 4.8 arcsec^2 and a mean surface brightness of $10.7 \text{ mag arcsec}^{-2}$, yielding 10,300 photon per frame. Eq. 5 suggests that in this case some correction might be obtained on objects as faint as 2,600 photon per frame, about $1.5 \text{ mag arcsec}^{-2}$ fainter, or roughly $12 \text{ mag arcsec}^{-2}$.

In astronomical terms, an object with surface brightness $m_I \sim 12 \text{ arcsec}^{-2}$ is not faint. Even on an 8 m telescope observing in the K band where the daytime sky is about magnitude 6 arcsec^{-2} ,¹⁹ the limiting surface brightness is about 13.6. Only with the advent of the ELTs will it be possible to approach potentially interesting surface brightnesses of 16 or 17 arcsec^{-2} in the visible and near IR bands during the day. It is worth noting that a tip-tilt natural guide star of the same brightness within the isokinetic angle of an object of interest would indeed allow access to even fainter sources, although the integration times required to overcome the high background are likely to be prohibitive in all cases but the most urgent targets of opportunity.

On the other hand, artificial satellites in low- and mid-Earth orbits seen in reflected sunlight will be accessible with this method. Since satellites move at non-sidereal rates it is not feasible to use natural stars as tip-tilt reference beacons; light from the object itself must be used. Satellite brightnesses depend strongly on the nature of the reflecting surface and the wavelength. On average, though, and regardless of their distance, satellites appear about as bright per unit solid angle

as the moon, or about magnitude 3 arcsec⁻². Solar-illuminated objects that are resolved by large telescopes dedicated to space situational awareness will therefore generally be observable.

6 References

1. J. M. Beckers and A. Cacciani, "Using laser beacons for daytime adaptive optics," *Exp. Astr.* **11**, 133–143 (2001).
2. A. Cacciani and A. M. Fofi, "The magneto-optical filter II: Velocity field measurements," *Sol. Phys.* **59**, 179–189 (1978).
3. C. Y. She, J. R. Yu, H. Latifi, and R. E. Bills, "High-spectral-resolution fluorescence light detection and ranging for mesospheric sodium temperature measurements," *Appl. Opt.* **31**(12), 2095–2106 (1992).
4. H. Chen, M. White, D. A. Krueger, and C. Y. She, "Daytime operation of Na temperature lidar using a dispersive Faraday vapor filter," in *Application of Lidar to Current Atmospheric Topics (Proc. SPIE)*, A. L. Sedlacek, Ed., **2833**, 46–52 (1996).
5. W. Kiefer, R. Löw, W. Jörg, and I. Gerhardt, "Na-Faraday rotation filtering: The optimal point," *Nature Scientific Reports* **4**(6552), 1–7 (2014).
6. M. Hart, S. M. Jefferies, and N. Murphy, "Daylight operation of a sodium laser guide star for adaptive optics wave-front sensing," *JATIS* **2**, doi:10.1117/1.JATIS.2.4.040501 (2016).
7. M. C. Roggemann, D. Douglas, E. Therikildsen, D. Archambault, R. Maeda, D. Schultz, and B. Wheeler, "Daytime image measurement and reconstruction for space situational awareness applications," in *Proc. AMOS Tech. Conf.*, S. Ryan, Ed. (2010).
8. F. Rigaut and E. Gendron, "Laser guide star in adaptive optics - the tilt determination problem," *Astron. Astrophys.* **261**, 677–684 (1992).
9. R. Davies, S. Rabien, C. Lidman, M. Le Louarn, M. Kasper, N. M. Förster Schreiber, V. Roccatagliata, N. Ageorges, P. Amico, C. Dumas, and F. Mannucci, "Laser guide star adaptive optics without tip-tilt," *Msngr.* **131**, 7–10 (2008).
10. C. Baranec, R. Riddle, N. M. Law, A. N. Ramaprakash, S. Tendulkar, K. Hogstrom, K. Bui, M. Burse, P. Chordia, H. Das, R. Dekany, S. Kulkarni, and S. Punnadi, "High-efficiency autonomous laser adaptive optics," *Astrophys. J.* **790**, L8–L13 (2014).
11. D. Gratadour, L. M. Mugnier, and D. Rouan, "Sub-pixel image registration with a maximum likelihood estimator," *Astron. Astrophys.* **443**, 357–365 (2005).
12. M. Guillaume, P. Melon, P. Réfrégier, and A. Llebaria, "Maximum-likelihood estimation of an astronomical image from a sequence at low photon levels," *J. Opt. Soc. Am. A* **15**, 2841–2848 (1998).
13. M. Hart, "Image registration for daylight adaptive optics," *Opt. Lett.* **43**, 1391–1394 (2018).
14. W. H. Press, S. A. Teukolsky, W. T. Vetterling, and B. P. Flannery, *Numerical Recipes in C, 2nd ed.*, ch. 10. CUP, Cambridge (1994).

15. L. C. Roberts and C. R. Neyman, "Characterization of the AEOS adaptive optics system," *Pub. Ast. Soc. Pac.* **114**, 1260–1266 (2002).
16. H. M. Martin, "Image motion as a measure of image quality," *Pub. Ast. Soc. Pac.* **99**, 1360–1370 (1987).
17. H. Lin and M. J. Penn, "The Advanced Technology Solar Telescope site survey sky brightness monitor," *Pub. Ast. Soc. Pac.* **116**, 652–666 (2004).
18. B. LaBonte, "Sky brightness measurements at Haleakala, 1955-2002," *Solar Physics* **217**, 367–381 (2003).
19. K. T. C. Jim, B. N. Gibson, and E. A. Pier, "Daytime sky brightness modeling of Haleakala along the GEO belt," in *Proc. AMOS Tech. Conf.*, S. Ryan, Ed. (2012).